

Biological Dose Estimation for Charged-Particle Therapy Using an Improved PHITS Code Coupled with a Microdosimetric Kinetic Model

Tatsuhiko Sato,^{a,1} Yuki Kase,^b Ritsuko Watanabe,^a Koji Niita^c and Lembit Sihver^{d,e}

^a Japan Atomic Energy Agency (JAEA), Tokai, Ibaraki 319-1195, Japan; ^b National Institute of Radiological Sciences (NIRS), Chiba 263-8555, Japan; ^c Research Organization for Information Science and Technology (RIST), Tokai, Ibaraki 319-1106, Japan; ^d Chalmers University of Technology, Göteborg, 412 96, Sweden; and ^e Roanoke College, Salem, Virginia

Sato, T., Kase, Y., Watanabe, R., Niita, K. and Sihver, L. Biological Dose Estimation for Charged Particle Therapy Using an Improved PHITS Code Coupled with a Microdosimetric Kinetic Model. *Radiat. Res.* 171, 107–117 (2009).

Microdosimetric quantities such as lineal energy, y , are better indexes for expressing the RBE of HZE particles in comparison to LET. However, the use of microdosimetric quantities in computational dosimetry is severely limited because of the difficulty in calculating their probability densities in macroscopic matter. We therefore improved the particle transport simulation code PHITS, providing it with the capability of estimating the microdosimetric probability densities in a macroscopic framework by incorporating a mathematical function that can instantaneously calculate the probability densities around the trajectory of HZE particles with a precision equivalent to that of a microscopic track-structure simulation. A new method for estimating biological dose, the product of physical dose and RBE, from charged-particle therapy was established using the improved PHITS coupled with a microdosimetric kinetic model. The accuracy of the biological dose estimated by this method was tested by comparing the calculated physical doses and RBE values with the corresponding data measured in a slab phantom irradiated with several kinds of HZE particles. The simulation technique established in this study will help to optimize the treatment planning of charged-particle therapy, thereby maximizing the therapeutic effect on tumors while minimizing unintended harmful effects on surrounding normal tissues. © 2009 by Radiation Research Society

INTRODUCTION

Approximately 50% of all cancer patients are cured of their disease, and approximately 40% of them are given radiotherapy as a part of their treatment. There is therefore a large and increasing population of cancer survivors previously exposed to radiation, and some of them are mani-

festing the longer-term effects of radiation on normal tissues. These effects can be deterministic, such as organ function loss based on fibrosis, atrophy and necrosis, or stochastic, such as secondary cancers. This can be very distressing to the patient and intractable to treatment. Thus it is of great importance to estimate doses in both the target tumor and the surrounding normal tissues to optimize the treatment planning for radiotherapy, thereby maximizing the therapeutic effect on the tumor while minimizing unintended harmful effects on normal tissues.

Recently, high-energy heavy ions (HZE particles) have been used for radiotherapy of tumors because of their high biological effectiveness. In the treatment planning for such charged-particle therapy, it is necessary to estimate not only the physical dose but also the biological dose, which is the product of the physical dose and relative biological effectiveness (RBE). In the Heavy-ion Medical Accelerator in Chiba (HIMAC) (1), the biological dose is estimated by a method proposed by Kanai *et al.* (2) that is based on the linear-quadratic (LQ) model with its parameters α and β determined by the dose distribution in terms of the unrestricted linear energy transfer (referred to hereafter as dose-LET distribution). Thus RBE is simply expressed as a function of LET in their model. However, the RBE of HZE particles cannot be uniquely determined from their LET because of their large cross sections for high-energy δ -ray production. Hence development of a biological dose estimation model that can explicitly consider the track structure of δ rays around the trajectory of HZE particles is urgently needed.

A number of studies, e.g. refs. (3–13), have been carried out to build such models. The theory of dual radiation action (TDRA) proposed by Kellerer and Rossi (4) is one of the most successful models in accounting for the biological effectiveness of ionizing radiation using microdosimetric quantities such as lineal energy, y , or specific energy, z . Using the microdosimetric concept, Scholz *et al.* established the local effect model (LEM) (6, 12), which is adopted in the treatment planning for heavy charged-particle therapy at GSI. The concept of TDRA was further developed in a microdosimetric kinetic (MK) model established

¹ Address for correspondence: Research Group for Radiation Protection, Division of Environment and Radiation Sciences, Nuclear Science and Engineering Directorate, Japan Atomic Energy Agency, Tokai, Naka, Ibaraki, 319-1195, Japan; e-mail: sato.tatsuhiko@jaea.go.jp.

by Hawkins (9, 10). The MK model was recently improved in terms of the saturation correction for expressing the decrease of RBE due to the overkill effect in very high y or z regions (11, 13). The improved MK model has succeeded in accounting for the cell survival curves under a variety of irradiation conditions using only one parameter, y^* , which can be obtained from the probability densities² of microdosimetric quantities measured with a tissue-equivalent proportional counter (TEPC). Establishment of a reliable simulation code to estimate the microdosimetric probability densities is the key issue in applying this model to the biological dose estimation for charged-particle therapy, since it is unfeasible to evaluate the probability densities experimentally inside the body of each patient.

Several Monte Carlo track-structure codes such as PARTRAC (14), PITS (15) and Gervais's code (16) are applicable to the estimation of the microdosimetric probability densities in the radiation fields of a certain monoenergetic HZE particle. On the other hand, the radiation fields in tumor and surrounding tissues in patients are rather complicated, since HZE particles can produce a variety of secondary particles in the human body by causing complex nuclear reactions. Furthermore, charged-particle therapy in HIMAC is carried out with spread-out Bragg peak (SOBP) carbon-ion beams, which are created by placing ridge filters at an upstream portion of the beam, and consequently the radiation fields of SOBP beams are composed of various kinds of particles over wide energy ranges. Thus the macroscopic calculation of fluences and energy spectra of HZE particles as well as the microscopic track-structure simulation around their trajectories is indispensable for the estimation of the microdosimetric probability densities in the region. However, none of the existing codes can handle both the macroscopic and microscopic simulations at once, since it is impractical to perform the microscopic track-structure simulation directly in the macroscopic codes because of computational-time limitations.

With these problems in mind, we have established a biological dose estimation method based on the MK model by developing a simulation code that enables us to calculate the microdosimetric probability densities in a macroscopic area of complex radiation fields. The outline of our strategy was as follows: (1) Calculate microdosimetric probability densities in liquid water around the trajectories of protons and several kinds of heavy ions with energies from 1 MeV/nucleon to 100 GeV/nucleon, using the microscopic electron-track-structure code TRACEL (17); (2) propose a mathematical function that can reproduce the simulation results to instantaneously predict the probability densities for all kinds of heavy ions over a wide energy range; (3) incorporate this function into the macroscopic particle trans-

port simulation code PHITS (18); and (4) evaluate the biological dose for charged-particle therapy based on the probability densities calculated by the improved PHITS code coupled with the MK model. The details of the first two procedures have already been reported in our previous paper (19). This paper therefore focuses on describing the last two items, including example results of biological dose estimation in PMMA slab and human voxel phantoms.

IMPROVEMENT OF THE PHITS CODE

Features of the PHITS Code

PHITS, the Particle and Heavy Ion Transport code System, can deal with the transport of all kinds of hadrons and heavy ions with energies up to 100 GeV/nucleon. The code can also treat the production, transport and decay of photons, electrons, positrons, pions, muons, kaons and various resonant states. The recent improvement of the code was described in detail in ref. (20).

The advantages of the code in the treatment planning for charged-particle ion therapy are that it is capable of (1) precisely calculating secondary particle spectra produced from nucleus-nucleus interactions, using a sophisticated nuclear-reaction model JQMD (21), (2) considering the influences of electromagnetic fields on the transports of charged particles, and (3) explicitly determining the energy of charged particles emitted from neutron-induced nuclear reactions, using the event generator mode (22) instead of the Kerma approximation. The first advantage is important in the dose estimation downstream of the Bragg peak, since the doses in this region are derived predominantly from the ionization due to the secondary particles. The second advantage enables us to perform the treatment planning for the beam transport through upstream apparatuses such as wobbler magnets, as described in ref. (23). The last advantage is indispensable for our purpose, since the microdosimetric probability densities are expressed as a function of the charge, energy and LET of ionizing particles and cannot be calculated directly from the neutron energy. Note that neutron transport simulation adopting the Kerma approximation, which is widely used for calculating the deposition energy due to lower-energy neutron transport, directly determines the mean value of the deposited neutron energies without specifying the charge and energy of the ionizing particles knocked out from the neutron interactions. Owing to these properties, we decided to improve the PHITS code to be capable of calculating the microdosimetric probability densities to apply the code to the biological dose estimation.

Incorporation of a Function for Calculating the Probability Densities of Microdosimetric Quantities into PHITS

Based on the model developed by Olko *et al.* (24), we proposed a function for expressing the energy-weighted probability density of deposition energy ε in spherical sites with diameter ϕ_s around a certain monoenergetic particle with charge Z , energy E and unrestricted LET in water L , as follows:

$$\begin{aligned} \varepsilon f_1(\varepsilon, \phi_s, Z, E, L) = & \frac{A(\phi_s, Z, E)\varepsilon^2}{\exp\{B(\phi_s, Z, E)[\varepsilon - C(\phi_s, Z, E)L\phi_s]\}} \\ & + \sum_{k=1}^2 \frac{\mu_k(\phi_s, Z, E)\varepsilon/w}{[j_k(\phi_s, Z, E) - 1]} \left[\frac{j_k(\phi_s, Z, E) - 1}{j_k(\phi_s, Z, E)} \right]^{\varepsilon/w} \\ & + \sum_{i=1}^6 P_i(\phi_s, Z, E)\delta(\varepsilon_{pi}) \\ & + \frac{P_7(\phi_s, Z, E)}{\sqrt{2\pi}\Gamma} \exp\left[-\frac{(\varepsilon - \varepsilon_{p7})^2}{2\Gamma^2}\right]. \end{aligned} \quad (1)$$

The procedures for deriving the function together with its verification

² There are two kinds of probability densities used in microdosimetry; one is energy-weighted probability density generally expressed as $yf_1(y)$, and the other is absorbed-dose probability density as $d_1(y)$. The two probability densities are proportional to each other, and they satisfy the normalization conditions $\int_0^\infty f_1(y) dy = 1$ and $\int_0^\infty d_1(y) dy = 1$, respectively.

were described in detail in our previous paper (19), and hence only a brief explanation of the features of the function is given in this paper. It should be noted that this function is identical to Eq. (7) in our previous paper (19), but the notations for some parameters are different from those used in its original form. For example, the notation z used in the previous paper is replaced by ε in this paper to distinguish clearly between the specific energy and the deposition energy.

The first two terms of the function are introduced for estimating the probability densities due to the direct ionization of the primary HZE particle and those of the secondary electrons, i.e. δ rays (referred to hereafter as direct and δ -ray contributions), respectively. The direct contribution is expressed by the distorted Fermi distribution, where the parameter A is the normalization constant and B and C indicate the magnitude of the distortion. The δ -ray contribution consists of two components indexed by k , where each term expresses the contributions from lower- and higher-energy δ rays, respectively. The parameter w denotes the average deposited energy per interaction, and thus ε/w represents the mean number of energy deposition events occurring in the site. In our calculation, the deposited energy due to the most frequent ionization, 10.9 eV, was chosen for the value of w . The parameters A , B , C , μ_k and j_k depend on the site diameter ϕ_s and the charge, Z , and energy, E , of the HZE particle. Their numerical values were determined from the least-squares fitting of the probability densities obtained from the Monte Carlo track-structure simulation using TRACEL (17), as described in our previous paper (19).

The last two terms in Eq. (1) are to reproduce sharp peak structures in the probability density at 10.9, 13.5, 17.0, 21.4, 26.3 and 533 eV and a broad peak around 700 eV. The first five peaks are triggered by the quantization of the threshold energies of excitations and the binding energy of each transition. The sharp peak at 533 eV is due to the production of the Auger electrons emitted from oxygen atoms, complementing the broad peak by coupling with several conventional energy deposition events. The sharp peak structure can be reproduced by Dirac's delta function, $\delta(\varepsilon_{pi})$, where ε_{pi} is the peak energy. On the other hand, it is assumed that the shape of the broad peak can be represented by a Gaussian distribution with a width Γ of 100 eV. The peak height, P_s , is dependent on the site diameter ϕ_s and the charge and energy of the HZE particle, and these numerical values were determined from the probability densities obtained from the Monte Carlo track-structure simulation.

The proposed function enables us to calculate the probability density of ε instantaneously with a precision equivalent to that of the Monte Carlo track-structure simulation that requires much computational time. We therefore incorporated this function, rather than the Monte Carlo track-structure simulation algorithm, into the PHITS code to estimate the microdosimetric probability densities in macroscopic matter. The improved PHITS can calculate the absorbed-dose probability densities of ε in spherical water sites with diameter ϕ_s , $d_1(\varepsilon, \phi_s)$, for a certain macroscopic region by numerically solving the equation

$$d_1(\varepsilon, \phi_s) = \sum_Z \int_E \int_L \frac{D(Z, E, L)}{D_T} \frac{\varepsilon f_1(\varepsilon, \phi_s, E, Z, L)}{\int_0^\infty \varepsilon f_1(\varepsilon, \phi_s, E, Z, L) d\varepsilon} dE dL, \quad (2)$$

where $D(Z, E, L)$ denotes the absorbed dose per unit energy and LET owing to the ionization of a particle with charge Z , energy E and LET L , while D_T denotes the total absorbed dose in the region. Both D and D_T can be estimated from the macroscopic particle transport simulation by PHITS. The absorbed-dose probability density of y , which is adopted in the biological dose estimation presented in the next section, can be obtained from $d_1(\varepsilon, \phi_s)$ by converting ε into y using their relationship $y = \varepsilon/l$, where l is the mean chord length of the site, $2\phi_s/3$. The improved PHITS can also calculate the absorbed-dose probability density of z , using the relationship $z = \varepsilon/m$, where m is the mass of the site. The site diameter ϕ_s , an input parameter of the code, can be arbitrarily specified to be from 1 nm to 2 μm .

It should be noted that the numerical values of the parameters used in Eq. (1) were determined only for water target sites with diameters from 1 nm to 2 μm , since we performed the Monte Carlo track-structure sim-

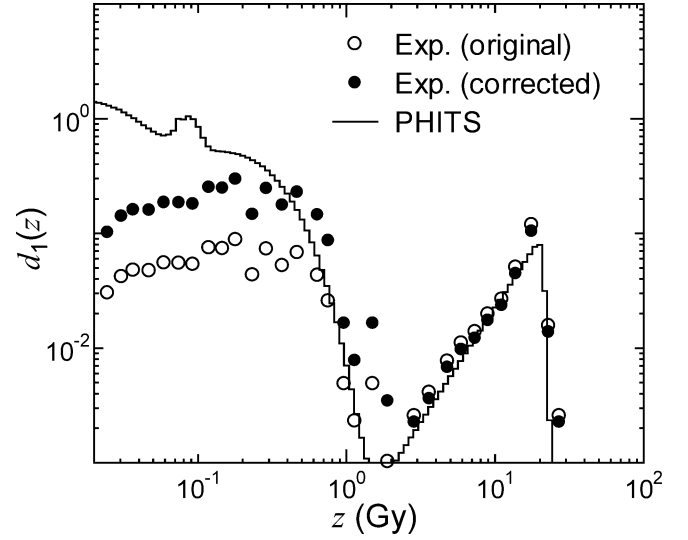


FIG. 1. Absorbed-dose probability densities of specific energy z around the trajectory of a 600 MeV/nucleon iron ion. The open and solid circles denote the original and corrected data measured with a wall-less TEPC (28), respectively, while the solid line represents the data calculated by the improved PHITS code.

ulation in water within a limited radial distance (19). Hence probability densities of microdosimetric quantities calculated by PHITS are always for water sites, although PHITS is able to calculate the total absorbed doses in every kind of material. However, this limitation does not pose a significant problem in the biological dose estimation, since the RBE of HZE particles is generally expressed by the probability density in water instead of that in the actual material.

Verification of the Accuracy of Microdosimetric Probability Densities Calculated by PHITS

In general, the accuracy of calculated microdosimetric probability densities can be verified by comparing the results with the corresponding experimental data measured with a TEPC. However, the experimental data measured with conventional TEPCs irradiated by HZE particles cannot be used for this purpose, since a large number of high-energy δ rays are produced in the wall of a TEPC so that this wall effect significantly changes the probability density away from the ideal condition, as discussed in many papers, e.g. refs. (25–27). Thus we compared the probability density measured in a wall-less TEPC irradiated with a 600 MeV/nucleon iron-ion beam (28) with the corresponding data calculated by the improved PHITS for the purpose of its verification. The wall-less TEPC was filled with propane gas, and the cylindrical site diameter and length simulated by this experiment was 1.3 μm .

The results of the comparison are presented graphically in Fig. 1. The original experimental data were given in terms of the energy-weighted probability density of z , $zf_1(z)$, but the data shown in this graph were converted to the absorbed-dose probability density of z , $d_1(z)$. Note that the statistical uncertainties in the calculated values shown in this paper are negligibly small. It is found from the graph that the direct and δ -ray contributions can be observed clearly at z values above and below 2 Gy, respectively, in both the calculated and measured probability densities, but a discrepancy can be observed between the ratios obtained from the calculation and from the experiment. This discrepancy is largely attributable to the limited radial distance covered by the experiment in which the probability density of z at the radial distances above 21.5 μm could not be measured. According to the radial-dose distribution models proposed independently by Magee *et al.* (29) and Chunxiang *et al.* (30), the dose deposited at the outer region of this measurement range is approximately 12% of the total for a 600 MeV/nucleon iron ion. Hence we

corrected the measured probability density, $d_{\text{im}}(z)$, by assuming that the probability density for the outer region is proportional to the measured data of the δ -ray contribution, in the relationship

$$d_{\text{ic}}(z) = \begin{cases} 0.88 + \frac{0.12}{\int_0^{z_T} d_{\text{im}}(z) dz} d_{\text{im}}(z) & (z < z_T) \\ 0.88 d_{\text{im}}(z) & (z \geq z_T), \end{cases} \quad (3)$$

where $d_{\text{ic}}(z)$ is the corrected probability density and z_T denotes the higher threshold of the z of the δ -ray contribution: 2 Gy in this case.

The corrected probability density is also depicted in Fig. 1. It is evident from the graph that the calculation can reproduce the corrected data very well except for those for z below 0.3 Gy. The peak in the calculated probability density at z around 0.08 Gy is triggered by the emission of the Auger electrons from excited oxygen atoms, and hence it is natural that the corresponding peaks cannot be observed in the experimental data measured with TEPCs filled with propane gas. The discrepancy at the lower- z region is probably due to the assumption adopted in the correction of the experimental data that the probability density for the outer region is proportional to the measured data of the δ -ray contribution. This assumption causes the underestimation of the corrected probability density at the very low- z region, since sites with such low z are expected to be scattered at locations far from the trajectory of the primary HZE particle, i.e. those at radial distances over the experimental limit. Thus our data correction is not enough to compensate for the increase of probability density at the low- z region. It should be noted, however, that the probability density at the low- z region generally does not play a significant role in the biological dose estimation. For instance, the dose-mean specific energies, z_{ID} , obtained from the calculated and corrected probability densities are in close agreement, 12.2 and 13.5 Gy, respectively, in spite of the existence of their large discrepancy at the low- z region. We therefore concluded that the microdosimetric probability densities calculated by the improved PHITS are precise enough to be used in the biological dose estimations shown in the next section.

BIOLOGICAL DOSE ESTIMATION

Methodology

The procedure for the biological dose estimation applying the MK model was described in detail in refs. (9–11, 13) together with its theoretical background. Hence only a methodological outline of the procedure is given in this paper.

According to the LQ model, the surviving fraction of cells irradiated with absorbed dose D can be expressed by the equation

$$S = \exp(-\alpha D - \beta D^2), \quad (4)$$

where S is the surviving fraction and α and β are parameters depending on the profile of the radiation such as energy, charge, speed and LET in a complicated manner. In the MK model, the parameter β can be regarded as a constant, and its numerical value can be obtained from the survival curve of the cells irradiated by a reference radiation—generally X rays. The parameter α can be estimated from the obtained β by the equation

$$\alpha = \alpha_0 + \beta z_{\text{ID}}^*, \quad (5)$$

where α_0 is a constant that represents the slope of the surviving fraction curve in the limit of LET = 0. The param-

eter z_{ID}^* denotes the saturation-corrected dose-mean specific energy for a subcellular structure referred to as domain. In the improved MK model (11, 13), z_{ID}^* can be calculated by the equation

$$\begin{aligned} z_{\text{ID}}^* &= \frac{l}{m} y^* \\ &= \frac{1}{\rho \pi r_d^2} y_0^2 \int_0^\infty \frac{1 - \exp(y^2/y_0^2)}{y} d(y, 2r_d) dy, \end{aligned} \quad (6)$$

where ρ and r_d are the density and radius of the domain, $d(y, 2r_d)$ is the absorbed-dose probability density of y for site diameter $2r_d$, and y_0 is a so-called saturation parameter that indicates the lineal energy above which the correction for the saturation due to the overkill effect becomes very important. The parameters z_{ID}^* and y^* are almost equal to the dose-mean specific energy and lineal energy, z_{ID} and y_{D} , respectively, in the cases where $d(y, 2r_d)$ in the region of high y is negligibly small, i.e., the approximation $\exp(y^2/y_0^2) = 1 - y^2/y_0^2$ is established even at the probability density of the maximum lineal energy. The saturation parameter y_0 can be calculated by the equation

$$y_0 = \frac{\rho \pi r_d R_n^2}{\sqrt{\beta(r_d^2 + R_n^2)}}, \quad (7)$$

where R_n is the radius of the nucleus of the target cell.

The MK model parameters r_d and α_0 are independent of the radiation type and dependent on the type of the target cell. Their numerical values can be determined from the surviving-fraction curves of the cell irradiated with X rays and a certain monoenergetic HZE particle whose saturation correction is negligibly small, i.e. $y^* \sim y_{\text{D}}$. For these radiations, the following simultaneous equations are established:

$$\alpha_x = \alpha_0 + \beta \frac{y_{\text{DX}}(2r_d)}{\rho \pi r_d^2} \quad \text{and} \quad (8)$$

$$\alpha_1 = \alpha_0 + \beta \frac{y_{\text{D1}}(2r_d)}{\rho \pi r_d^2}, \quad (9)$$

where α_x and α_1 are the measured α values and $y_{\text{DX}}(2r_d)$ and $y_{\text{D1}}(2r_d)$ are the dose-mean lineal energies for site diameter $2r_d$ upon X and HZE-particle irradiation, respectively. Solving the simultaneous equations, we can calculate the MK model parameters r_d and α_0 by the equations

$$r_d = \sqrt{\frac{\beta[y_{\text{D1}}(2r_d) - y_{\text{DX}}(2r_d)]}{\rho \pi (\alpha_1 - \alpha_x)}} \quad \text{and} \quad (10)$$

$$\alpha_0 = \alpha_x - \left[\frac{\alpha_1 - \alpha_x}{y_{\text{D1}}(2r_d) - y_{\text{DX}}(2r_d)} \right] y_{\text{DX}}(2r_d). \quad (11)$$

Substituting these parameters into Eq. (7), the saturation parameter y_0 can be determined.

The parameter α for a complex radiation field, α_c , can be estimated from Eqs. (5) and (6), inserting the obtained

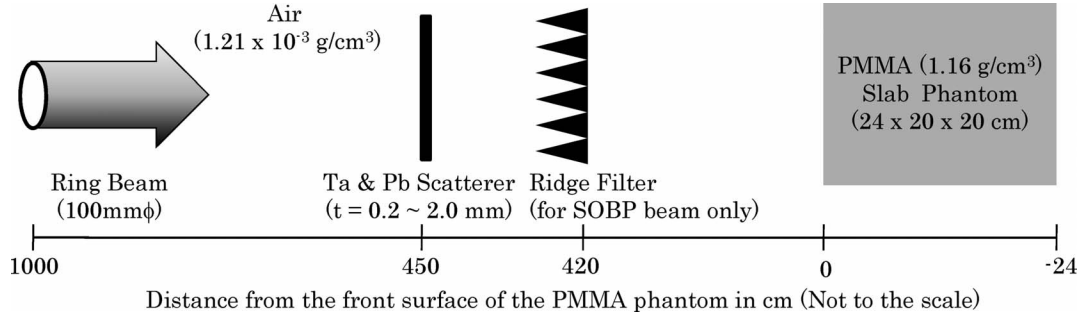


FIG. 2. Simulation setup for the biological dose estimation in a PMMA slab phantom.

MK model parameters and $d(y, 2r_d)$ calculated by the improved PHITS. Using α_c , the dose of the surviving fraction S in the complex radiation field, $D_c(S)$ can be determined by the equation

$$D_c(S) = \frac{-\alpha_c + \sqrt{\alpha_c^2 - 4\beta \ln(S)}}{2\beta}. \quad (12)$$

The RBE for surviving fraction S in the complex radiation field can be obtained simply by the equation

$$\text{RBE}_c(S) = \frac{D_x(S)}{D_c(S)}, \quad (13)$$

where $D_x(S)$ is the X-ray dose for surviving fraction S , which can be obtained from Eq. (12) by replacing α_x by α_c . Finally, we can estimate the biological dose as the product of the RBE and the physical dose, which can be calculated from the macroscopic particle transport simulation of PHITS.

Biological Dose Estimation in a Slab Phantom

To prove the applicability of this method to the treatment planning of charged-particle therapy in HIMAC, we performed a simulation estimating the biological dose in a PMMA slab phantom irradiated by SOBP carbon-ion beams as well as several kinds of monoenergetic HZE-particle beams. Figure 2 shows the simulation setup for the biological dose estimation, and Table 1 summarizes the profiles of the irradiation beams. The biological end point

adopted in the estimation was a 10% surviving fraction for human salivary gland (HSG) tumor cells. These conditions are the same as those adopted in the experimental biological dose estimation using a conventional TEPC (11).

Preceding the simulation for estimating the biological dose in the slab phantom, we must determine the parameters used in the MK model. We adopted the same values used in ref. (11) for the domain density ρ , the nuclear radius R_n , and the β parameter; that is, $\rho = 1.0 \text{ g/cm}^3$, $R_n = 4.1 \text{ } \mu\text{m}$, and $\beta = 0.05 \text{ Gy}^{-2}$, respectively. The α parameters for X rays and a certain monoenergetic HZE-particle irradiations, α_x and α_i , were set to 0.192 and 0.332 Gy^{-1} , respectively, which were evaluated from the least-squares fitting of the experimental surviving fractions of the HSG cells (11) considering the experimental uncertainties. Note that carbon ions with energy 290 MeV/nucleon were employed as representative monoenergetic HZE particles, as in ref. (11). The domain radius r_d can be obtained by numerically solving Eq. (10) using these parameters coupled with y_{DX} and y_{DI} calculated by the improved PHITS. In solving the equation, we adopted the Newton method, since the calculated y_{DX} and y_{DI} depend on r_d in a complicated manner. The numerical value of the estimated r_d is 0.300 μm , and y_{DX} and y_{DI} for this domain radius are 4.04 and 8.99 $\text{keV}/\mu\text{m}$, respectively. Substituting these parameters into Eqs. (7) and (11), we obtained the values of 108 $\text{keV}/\mu\text{m}$ and 0.0777 Gy^{-1} for y_0 and α_0 , respectively. It should be noted that the parameters evaluated are different from those obtained by Kase *et al.* (11), who adopted the y_D

TABLE 1
Beam Conditions Adopted in the Biological Dose Estimation in a PMMA Slab Phantom, Together with the Depths at which the Measured Value of the HSG Cell is Available in the Phantom

Incident particle	Monoenergetic or SOBP	Material and thickness of scatterer (mm)	Range in PMMA ^a (g/cm ²)	Depth at which α value was measured (g/cm ²)
Carbon, 290 MeV/nucleon	Monoenergetic	Tantalum, 0.434	14.8	0.1, 13.4, 14.5, 14.7, 14.8, 14.9, 15.0
Carbon, 290 MeV/nucleon	SOBP ^b	Tantalum, 0.649	9.2–14.8	0.33, 9.4, 11.8, 14.3, 14.6
Carbon, 400 MeV/nucleon	SOBP	Tantalum, 0.754	18.8–24.9	19.8, 22.2, 24.8
Neon, 230 MeV/nucleon	Monoenergetic	Tantalum, 0.539	5.1	0.1, 3.6, 4.3, 4.6
Silicon, 490 MeV/nucleon	Monoenergetic	Lead 1.6 Tantalum, 0.434	13.5	0.1, 12.5, 13.0, 13.1, 13.4, 13.45, 13.5, 13.55
Iron, 200 MeV/nucleon	Monoenergetic	Tantalum, 0.215	0.9	0.1, 0.38, 0.78, 0.84
Iron, 500 MeV/nucleon	Monoenergetic	Lead, 1.6 Tantalum, 0.215	7.1	0.33

^a Range for HZE particles in front of the slab phantom.

^b Spread-out Bragg peak.

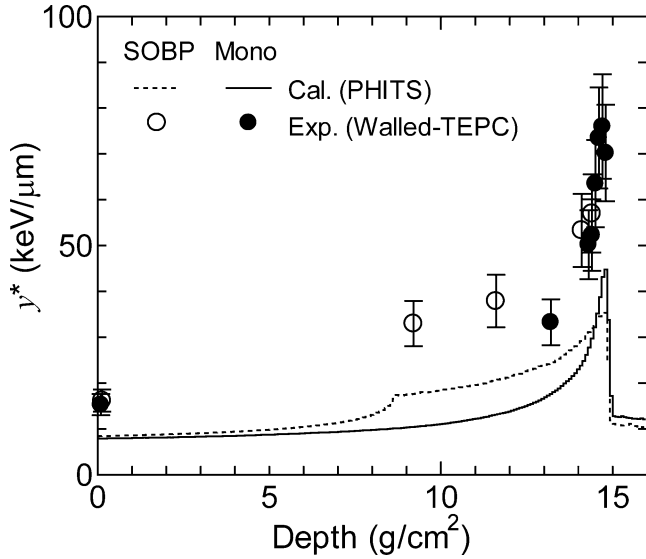


FIG. 3. Calculated and measured y^* for monoenergetic and SOBP 290 MeV/nucleon carbon-ion beams as a function of the depth in a PMMA slab phantom. The experimental data are taken from ref. (11).

measured by a conventional TEPC in the parameter determination. This discrepancy is largely due to the wall effect on the probability density measured by the TEPC, since the wall effect raises the measured y_D for high-energy particles greatly. For instance, y_D measured by a walled TEPC is estimated to be 1.34 times larger than that by a wall-less TEPC in the case of 45 MeV/nucleon argon ions, based on the simulation of Nikjoo (25), and this ratio is expected to be larger for higher-energy particles.

Using our evaluated MK model parameters, we estimated y^* , α and the biological dose in the slab phantom irradiated by the HZE-particle beams listed in Table 1, based on the $d(y, 2r_d)$ calculated by the improved PHITS code. As examples of the results, the calculated y^* for the monoenergetic and SOBP 290 MeV/nucleon carbon-ion beams are depicted in Fig. 3 as a function of the depth in the phantom. The corresponding experimental data obtained by Kase *et al.* (11) are also plotted in the figure. It is clear from the graphs that y^* becomes larger in the Bragg-peak and SOBP regions, indicating higher RBEs there. Note that the calculated y^* are much smaller than the corresponding measured data. This discrepancy also was due to the wall effect in the experimental data.

Figure 4 shows the measured α at several depths in the phantom as a function of the calculated y^* at the corresponding locations. The depths at which the measurements were performed are tabulated in Table 1. The relationship between α and y^* resulting from Eq. (5) with our obtained MK model parameters is also shown in the figure. It is evident from the graph that the α calculated by Eq. (5) agrees with the measured data very well except for a few data obtained from the monoenergetic 200 MeV/nucleon iron-ion irradiation. This agreement verifies that RBE of the varieties of HZE particles can be estimated simply from

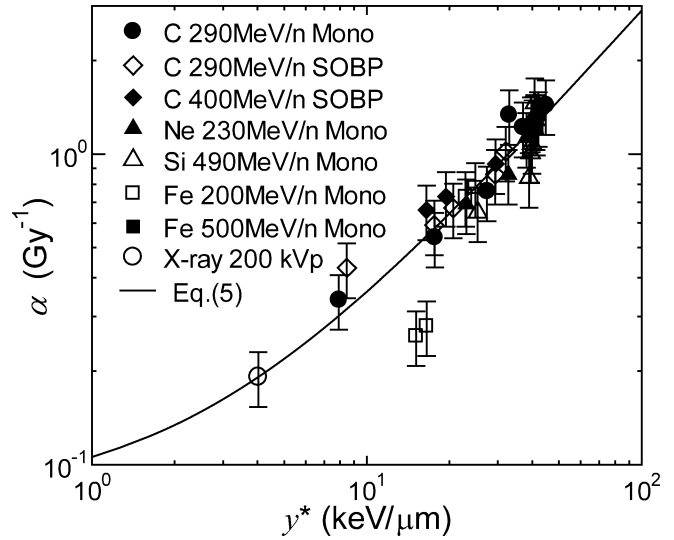


FIG. 4. Measured α values at several depths in the PMMA slab phantom (11) as a function of the calculated y^* at the locations. The solid line denotes the relationship between α and y^* expected from Eq. (5). The depths at which the measurements were performed are tabulated in Table 1.

only one parameter, y^* , indicating the applicability of the biological dose estimation method using y^* to complex radiation fields. The exceptions are observed in the data measured around the Bragg peak of the beam. This discrepancy is probably due to a slight difference between the experimental and simulation setups, since y^* around the Bragg peak for iron ions changes dramatically according to the depth at which the measurement of y^* is performed. For instance, the calculated y^* at only 0.05 g/cm² upstream or downstream of the Bragg peak is approximately twice that at the peak, and it is very difficult to reproduce such experimental conditions with accuracy in the simulation. Furthermore, the depths at which the TEPC was located in the measurements also had uncertainties of approximately 0.05 g/cm² due to the round shape of the detector.

Figure 5 shows a comparison between the RBEs where there is a 10% surviving fraction of irradiated HSG cells estimated from the α values obtained by Kase *et al.* (11) and our simulation under different irradiation conditions. The data are plotted as a function of the depth in the phantom. It is evident from the graph that our simulation can reproduce the experimental data at various locations, as could be expected from Fig. 4. The sudden decreases of the calculated RBE at the Bragg peaks of the monoenergetic neon- and iron-ion irradiations are triggered by the saturation correction for the overkill effect. This effect was also observed in the experimental data for the iron-ion irradiation, although the depths at which the effect was measured were slightly different from the calculated data, as described before.

Figure 6 shows the calculated biological and physical doses for the monoenergetic and SOBP 290 MeV/nucleon carbon-ion beams as a function of the depth in the phantom.

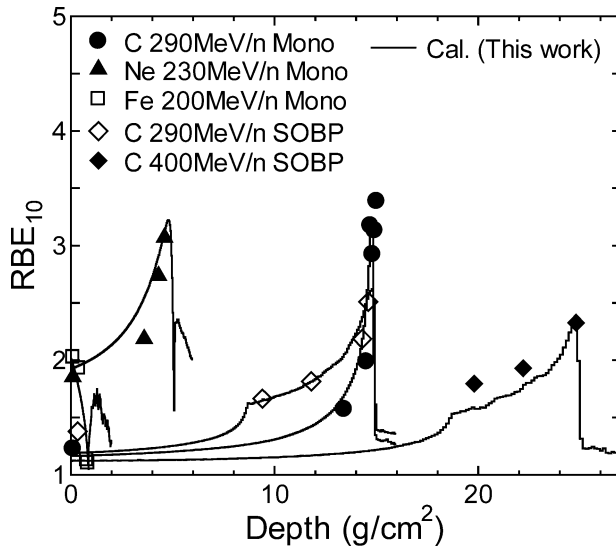


FIG. 5. Comparison between the RBEs for the 10% surviving fraction of the HSG cell estimated from the α values obtained by Kase *et al.* (11) and our simulation for several irradiation conditions.

The depth-dose distributions in a water phantom irradiated by the same beams measured by an ionization chamber (31) are also plotted in the graphs. The measured distributions are normalized to the calculated physical doses at the front surface and at the 5 g/cm² depth of the phantom for the monoenergetic and SOBP beams, respectively. It is evident from the graphs that our simulation can reproduce the measured physical doses very well even downstream of the Bragg peak. This indicates the accuracy of the PHITS calculation in terms of the secondary particle spectra produced by nuclear reactions of HZE particles, since doses in the region are deposited largely by the ionization by the secondary particles. The agreement between the measurements and calculations of both RBE and physical dose as shown in Figs. 5 and 6, respectively, proves the reliability of the biological dose estimation method we developed, since the biological dose is the product of the two quantities.

The ridge filter mounted at the upstream portion of the SOBP beam was designed to achieve a constant biological dose region over 6 g/cm² in width, using the one-dimensional HZE-particle transport code HIBRAC (32) coupled with the LET-based LQ model proposed by Kanai *et al.* (2), as also shown in Fig. 6. However, the biological doses obtained by PHITS coupled with the MK model are not constant at the SOBP region; the value at the proximal region of the beam is approximately 5% higher than that at the distal region. This discrepancy is attributed not to the difference between the biological dose estimation models themselves but rather to the difference between the simulation codes adopted in the estimation, since one-dimensional codes tend to overestimate the dose at a distal region due to the ignorance of the lateral divergence of the dose, as discussed in ref. (31). It should also be mentioned that

HIBRAC was recently improved³ by updating the reaction cross-section model (33), but this updated version was not used in the calculation of the Kanai model shown in this paper.

To clarify the difference between the MK and Kanai models, we estimated the biological doses based on the Kanai model using the dose-LET distributions calculated by PHITS instead of HIBRAC. The results are also shown in the graphs. It is evident from the graphs that the biological doses calculated by PHITS coupled with the MK and Kanai models are almost identical to each other for the monoenergetic beam. For the SOBP beam, the calculation employing the MK model gives slightly higher values than that using the Kanai model, especially at the SOBP region. This slight disagreement is due to the difference between the biological dose estimation models as well as that between the target cells employed in the parameter determination of the models.

An advantage of the MK model compared to Kanai model is that it makes a biological dose estimation feasible by taking the difference among RBEs for each type of the tumor cell into consideration. This is because the MK model is fully based on the theoretical background, and its parameters can be determined from the surviving fraction curves of target cells irradiated by only two types of radiation: X rays and monoenergetic carbon ions with energy 290 MeV/nucleon in our case. On the other hand, the Kanai model is an empirical method that requires a large number of experiments for measuring the surviving fraction curves of a target cell irradiated by varieties of HZE particles over a wide energy range to determine the LET dependence of the parameters used in the model.

Biological Dose Estimation in a Human Voxel Phantom

The biological dose estimation method based on the improved PHITS code coupled with the MK model has great advantages when applied to treatment planning for charged-particle therapy, since it enables us to estimate the biological doses not only in a tumor but also in surrounding normal tissues, considering the effects of secondary particles produced in upstream apparatuses as well as inside the human body. Furthermore, PHITS can model voxel phantoms of a human body built from the CT scan data of each patient. We therefore performed simulations for estimating the biological doses in several tissues of a Japanese male voxel phantom JM (34) irradiated by an SOBP 290 MeV/nucleon carbon-ion beam.

A schematic simulation setup is illustrated in Fig. 7. The pencil monoenergetic beam was broadened by a wobbler magnet. The broadened beam successively passed through a scatterer, a ridge filter and a lead collimator with a 5 × 5-cm² hole and struck the head of a voxel phantom from

³L. Sihver and D. Mancusi, HIBRAC: a 1-D deterministic heavy-ion transport code optimised for radiotherapy. Manuscript submitted for publication.

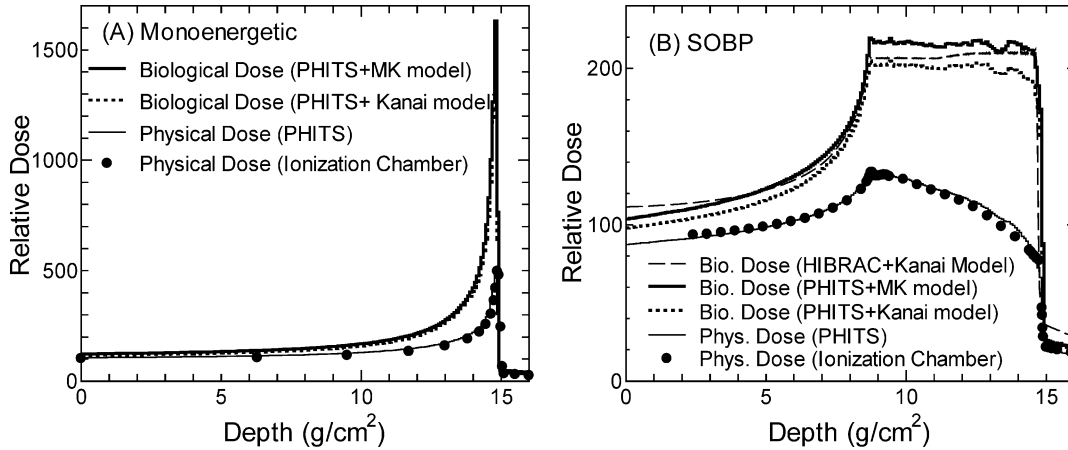


FIG. 6. Biological and physical doses for (panel A) monoenergetic and (panel B) SOBP 290 MeV/nucleon carbon-ion beams as a function of the depth in the PMMA slab phantom. The solid circles denote the normalized depth-dose distribution in water measured by an ionization chamber (31).

the lateral direction. In the simulation, we calculated the physical doses, dose equivalents using the $Q(L)$ and $Q(y)$ relationships defined in ICRP Report 60 (35) and ICRU Report 40 (36), respectively, as well as the biological dose based on the MK model. According to ICRP Report 92 (37), one reason for introducing the LET-based quality factor $Q(L)$ instead of the y -based relationship $Q(y)$ that had already been defined in ICRP Report 40 was that LET was more convenient in computations, although y is definitely a better index for expressing the quality factor. Hence it is worthwhile to compare the $Q(L)$ - and $Q(y)$ -based dose equivalents, where the latter can be calculated using only the improved PHITS code.

The results of the simulation are summarized in Table 2. The statistical errors in the values are generally small—less than 2% in most cases. The data are normalized to achieve a 10% surviving fraction of the HSG tumor cells in the SOBP; i.e., the biological dose in the region is set equal to $D_x(0.1)$. The dose in the target organ, the brain, is much higher than for other tissues and organs, indicating the high concentration of dose with this heavy charged-particle therapy. Among the non-target tissues, the doses to tissues distributed widely in the human body such as bone marrow

and skin are relatively high in comparison to the others, since some parts of these tissues are directly irradiated by the primary HZE particles. The doses for the other tissues simply decrease with increasing distance from that tissue to the target organ. The biological doses in each tissue are smaller than the corresponding dose equivalents, since the biological end points employed in the dose estimations are different from each other. In general, the RBEs of HZE particles for cell killing are smaller than those for chromosome aberrations. The former and latter are correlated to the biological dose and the dose equivalent, respectively.

The $Q(L)$ -based dose equivalents are larger than the corresponding $Q(y)$ -based values for tissues directly irradiated by the primary HZE particles, while the relationship is reversed for the other tissues. For low-energy charged particles, one can assume the relationship between dose-mean lineal energy y_D for site diameter $1 \mu\text{m}$ and LET L to be (38)

$$y_D = 9L/8 + 0.75 \text{ (keV}/\mu\text{m}). \quad (14)$$

Under this assumption, the $Q(y)$ defined in ICRU Report 40 can simply be converted to the LET-based quality factor, and its numerical values are slightly larger than the $Q(L)$

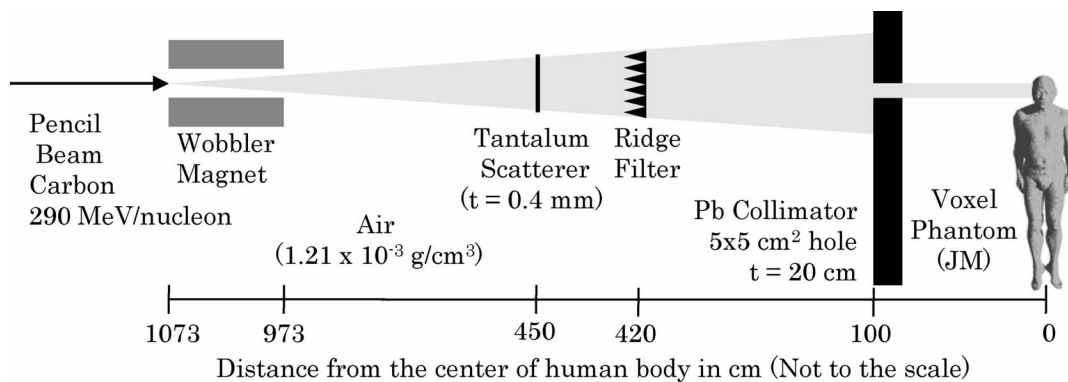


FIG. 7. Simulation setup for the biological dose estimation in a human voxel phantom.

TABLE 2
Calculated Physical and Biological Doses, and Dose Equivalents in Several Important Tissues in the JM Phantom Irradiated by a Carbon 290 MeV/Nucleon SOBPs Beam

	Physical dose (mGy)	Biological dose (mGy-Eq.)	$Q(L)$ -based dose equivalent (mSv)	$Q(y)$ -based dose equivalent (mSv)
Effective ^a	2.25	3.13	10.8	9.61
Bone marrow	16.8	23.4	81.3	71.9
Breast	0.0840	0.170	0.716	0.766
Colon	0.0381	0.0667	0.258	0.276
Lungs	0.0582	0.0882	0.287	0.305
Stomach	0.0519	0.0879	0.322	0.348
Gonads	0.00908	0.0204	0.0936	0.0969
Liver	0.0345	0.0465	0.138	0.147
Esophagus	0.0969	0.136	0.397	0.419
Thyroid	0.162	0.230	0.719	0.752
Bladder	0.0152	0.0224	0.0672	0.0742
Bone surface	10.3	14.4	50.0	44.2
Brain	707	1146	5254	4280
Salivary	1.09	1.34	3.06	3.01
Skin	5.36	6.61	16.1	15.8
Remainder tissues	0.226	0.281	0.743	0.737

Notes. The simulation setup for this calculation is illustrated in Fig. 7. The data are normalized to achieve a 10% surviving fraction of HSG tumor cells in the SOBPs region.

^a Sum of tissue doses weighted by w_T , excluding the brain contribution.

defined in ICRP Report 60 except for very high-LET region, as shown in Fig. 4.1 of ICRP Report 92. The doses in tissues far from the target organ are deposited predominantly by low-energy charged particles emitted from neutron-induced reactions, and hence it is natural that the $Q(y)$ -based dose equivalents in those tissues are slightly larger than the corresponding $Q(L)$ -based values. On the other hand, y_D is expected to be much smaller than that calculated by Eq. (14) for HZE particles because of their large production cross sections of high-energy δ rays. Thus the numerical value of $Q(L)$ is generally larger than the mean value of $Q(y)$ for HZE particles with LET or y below 100 keV/ μ m. This is why the $Q(L)$ -based dose equivalents are larger than the corresponding $Q(y)$ -based values for tissues directly irradiated by the primary HZE particles. When the $Q(L)$ - and $Q(y)$ -based dose equivalents are apparently different from each other, as is the case here, it is better to use $Q(y)$ -based dose equivalents in the relative risk estimation, since $Q(L)$ was introduced just to be mathematically in line with the curve obtained from $Q(y)$ coupled with Eq. (14), as described in ICRP Report 92.

One purpose of evaluating doses in normal tissues in the treatment planning is to estimate the risk of inducing stochastic effects such as secondary cancer, and the dose equivalents are better indexes for this risk estimation than the other calculated values. We therefore calculated the effective dose equivalents from the obtained dose equivalents in each tissue coupled with the tissue weighting factor w_T defined in ICRP Report 103 (39). In this calculation, we set the tissue weighting factor for the brain to be 0, since the brain is the target organ whose stochastic effect need not be considered in our simulation. The result is also given in Table 2, together with the effective physical and biolog-

ical doses obtained in the same manner as described above. The $Q(L)$ -based effective dose equivalent is larger than the corresponding $Q(y)$ -based value, indicating the overestimation of the risk of charged-particle therapy if one employs LET as an index for expressing the quality factor. The calculated effective dose equivalents are almost the same as the effective dose from a whole-body CT scan, which is expected to be 8 to 20 mSv under certain conditions (40). However, this coincidence is not evidence enough to conclude that the risks of induction of secondary cancers by charged-particle therapy and CT scans are almost equivalent, since the effective dose equivalent from charged-particle therapy depends significantly on the irradiation conditions such as the charge and energy of the incident particles, the structure of upstream apparatuses, and the location of the target tumor. Furthermore, the effect of non-uniform exposure must be considered in the risk estimation, since the dose from heavy charged-particle therapy is concentrated in a small area around the target tumor. More systematic studies estimating the risks of induction of secondary cancer by charged-particle therapy are desired.

CONCLUSIONS

The macroscopic particle transport code PHITS was improved to estimate the probability densities of microdosimetric quantities in complex radiation fields by incorporating a mathematical function that can instantaneously calculate the probability densities around the trajectory of all kinds of HZE particles. Using the improved PHITS code, we have established a new method for estimating biological dose from charged-particle therapy based on the microdos-

imetric kinetic model. In this method, the biological dose can be determined by multiplying the physical dose by the RBE for the surviving fraction of tumor cells. The physical dose is calculated from the macroscopic particle transport simulation by PHITS, while the RBE is estimated from the saturation-corrected dose-mean lineal energy y^* that is calculated from the absorbed-dose probability density of y with a mathematical function incorporated in PHITS. The accuracy of the biological dose estimated by this method was tested by comparing the calculated physical dose and RBE data with the corresponding experimental values obtained by irradiating a slab phantom with SOBP carbon-ion beams as well as several monoenergetic HZE particles.

An advantage of applying this method to the treatment planning of charged-particle therapy is that it enables us to lump calculations for all the required tasks together into one simulation, such as the design of upstream apparatuses, the estimation of biological dose in a tumor, and estimation of dose equivalents in surrounding normal tissues. As an example, we calculated the $Q(L)$ - and $Q(y)$ -based effective dose equivalents as indexes for the risk of stochastic effects from charged-particle therapy for a certain case and obtained a value comparable to the effective dose from a whole-body CT scan. Further studies are desired for estimating the normal-tissue complications such as the risk of induction of secondary cancers by charged-particle therapy. The development of a model for correlating the microdosimetric probability densities with chromosome aberration or DNA damage is a key issue for risk estimation. The simulation technique established in this study is also capable of contributing to the health risk estimation of astronauts exposed to cosmic rays, an area requiring additional study.

ACKNOWLEDGMENTS

We would like to thank Dr. D. Satoh, Dr. K. Sato and Dr. A. Endo for their support in incorporating the human voxel phantom into PHITS.

Received: June 20, 2008; accepted: August 13, 2008

REFERENCES

1. Y. Hirao, H. Ogawa, S. Yamada, Y. Sato, T. Yamada, K. Sato, A. Itano, M. Kanazawa, K. Noda and S. Matsumoto, Heavy ion synchrotron for medical use—HIMAC project at NIRS-JAPAN. *Nucl. Phys. A* **538**, 541c–550c (1992).
2. T. Kanai, Y. Furusawa, K. Fukutsu, H. Itsukaichi, K. Eguchi-Kasai and H. Ohara, Irradiation of mixed beam and design of spread-out Bragg peak for heavy-ion therapy. *Radiat. Res.* **147**, 78–85 (1997).
3. J. J. Butts and R. Katz, Theory of RBE for heavy ion bombardment of dry enzymes and viruses. *Radiat. Res.* **30**, 855–871 (1967).
4. A. M. Kellerer and H. H. Rossi, A generalized formation of dual radiation action. *Radiat. Res.* **75**, 471–488 (1978).
5. M. Zaider and H. H. Rossi, The synergistic effects of different radiations. *Radiat. Res.* **83**, 732–739 (1980).
6. M. Scholz, A. M. Kellerer, W. Kraft-Weyrather and G. Kraft, Computation of cell survival in heavy ion beams for therapy. *Radiat. Environ. Biophys.* **36**, 59–66 (1997).
7. F. A. Cucinotta, H. Nikjoo and D. T. Goodhead, Applications of amorphous track models in radiation biology. *Radiat. Environ. Biophys.* **38**, 81–92 (1999).
8. P. E. Briden, P. D. Holt and J. A. Simmons, The track structures of ionizing particles and their application to radiation biophysics. *Radiat. Environ. Biophys.* **38**, 175–184 (1999).
9. R. B. Hawkins, A statistical theory of cell killing by radiation of varying linear energy transfer. *Radiat. Res.* **140**, 366–374 (1994).
10. R. B. Hawkins, A microdosimetric-kinetic model for the effect of non-Poisson distribution of lethal lesions on the variation of RBE with LET. *Radiat. Res.* **160**, 61–69 (2003).
11. Y. Kase, T. Kanai, Y. Matsumoto, Y. Furusawa, H. Okamoto, T. Asaba, M. Sakama and H. Shinoda, Microdosimetric measurements and estimation of human cell survival for heavy-ion beams. *Radiat. Res.* **166**, 629–638 (2006).
12. T. Elsasser and M. Scholz, Cluster effects within the local effect model. *Radiat. Res.* **167**, 319–329 (2007).
13. Y. Kase, T. Kanai, N. Matsufuji, Y. Furusawa, T. Elsasser and M. Scholz, Biophysical calculation of cell survival probabilities using amorphous track structure models for heavy-ion irradiation. *Phys. Med. Biol.* **53**, 37–59 (2008).
14. M. Dingfelder, M. Inokuti and H. G. Paretzke, Inelastic-collision cross sections of liquid water for interactions of energetic protons. *Radiat. Phys. Chem.* **59**, 255–275 (2000).
15. W. E. Wilson and H. Nikjoo, A Monte Carlo code for positive ion track simulation. *Radiat. Environ. Biophys.* **38**, 97–104 (1999).
16. B. Gervais, M. Beuve, G. H. Olivera and M. E. Galassi, Numerical simulation of multiple ionization and high LET effects in liquid water radiolysis. *Radiat. Phys. Chem.* **75**, 493–513 (2006).
17. H. Tomita, M. Kai, T. Kusama and A. Ito, Monte Carlo simulation of physicochemical processes of liquid water radiolysis. *Radiat. Environ. Biophys.* **36**, 105–116 (1997).
18. H. Iwase, K. Niita and T. Nakamura, Development of a general-purpose particle and heavy ion transport Monte Carlo code. *J. Nucl. Sci. Technol.* **39**, 1142–1151 (2002).
19. T. Sato, R. Watanabe and K. Niita, Development of a calculation method for estimating specific energy distribution in complex radiation fields. *Radiat. Prot. Dosimetry* **122**, 41–45 (2006).
20. K. Niita, T. Sato, H. Iwase, H. Nose, H. Nakashima and L. Sihver, Particle and heavy ion transport code system; PHITS. *Radiat. Meas.* **41**, 1080–1090 (2006).
21. K. Niita, S. Chiba, T. Maruyama, H. Takada, T. Fukahori, Y. Nakahara and A. Iwamoto, Analysis of the (N,xN) reactions by quantum molecular dynamics plus statistical decay model. *Phys. Rev.* **C52**, 2620 (1995).
22. T. Sato, S. Tsuda, Y. Sakamoto, Y. Yamaguchi and K. Niita, Analysis of dose-LET distribution in the human body irradiated by high energy hadrons. *Radiat. Prot. Dosimetry* **106**, 145–153 (2003).
23. H. Nose, K. Niita, M. Hara, K. Uematsu, O. Azuma, Y. Miyauchi, M. Komori and T. Kanai, Improvement of three-dimensional Monte-Carlo code PHITS for heavy ion therapy. *J. Nucl. Sci. Technol.* **42**, 250–255 (2005).
24. P. Olko and J. Booz, Energy deposition by protons and alpha particles in spherical sites of nanometer to micrometer diameter. *Radiat. Environ. Biophys.* **28**, 1–17 (1990).
25. ICRU, *Microdosimetry*. Report 36, International Commission on Radiation Units and Measurements, Bethesda, MD, 1983.
26. H. Nikjoo, I. K. Khvostunov and F. A. Cucinotta, The response of tissue-equivalent proportional counters to heavy ions. *Radiat. Res.* **157**, 435–445 (2002).
27. S. B. Guetersloh, T. B. Borak, P. J. Taddei, C. Zeitlin, L. Heilbronn, J. Miller, T. Murakami and Y. Iwata, The response of a spherical tissue-equivalent proportional counter to different ions having similar linear energy transfer. *Radiat. Res.* **161**, 64–71 (2004).
28. N. F. Metting, H. H. Rossi, L. A. Braby, P. J. Kliauga, J. Howard, M. Zaider, W. Schimmerling, M. Wong and M. Rapkin, Microdosimetry near the trajectory of high-energy heavy ions. *Radiat. Res.* **116**, 183–195 (1988).

29. J. L. Magee and A. Chatterjee, Radiation chemistry of heavy-particle tracks 1. General considerations. *J. Phys. Chem.* **84**, 3529–3536 (1980).
30. Z. Chunxiang, D. E. Dunn and R. Katz, Radial distribution of dose and cross-sections for the inactivation of dry enzymes and viruses. *Radiat. Prot. Dosimetry* **13**, 215–218 (1985).
31. Y. Kase, N. Kanematsu, T. Kanai and N. Matsufuji, Biological dose calculation with Monte Carlo physics simulation for heavy-ion radiotherapy. *Phys. Med. Biol.* **51**, N467–N475 (2006).
32. L. Sihver, D. Schardt and T. Kanai, Depth-dose distributions of high-energy carbon, oxygen and neon beams in water. *Jpn. J. Med. Phys.* **18**, 1–21 (1998).
33. L. Sihver, C. H. Tsao, R. Silberberg, T. Kanai and A. F. Barghouty, Total reaction and partial cross section calculations in proton-nucleus ($Z_t < 26$) and nucleus-nucleus reactions (Z_p and $Z_t < 26$). *Phys. Rev. C* **47**, 1225–1236 (1993).
34. K. Sato, H. Noguchi, Y. Emoto, S. Koga and K. Saito, Japanese adult male voxel phantom constructed on the basis of CT-images. *Radiat. Prot. Dosimetry* **123**, 337–344 (2007).
35. ICRP, *1990 Recommendations of the International Commission on Radiological Protection*. Publication 60, *Annals of the ICRP*, Vol. 21, Nos. 1–3, Pergamon Press, Oxford, 1991.
36. ICRU, *The Quality Factor in Radiation Protection*. Report 40, International Commission on Radiation Units and Measurements, Bethesda, MD, 1986.
37. ICRP, *Relative Biological Effectiveness (RBE), Quality Factor (Q), and Radiation Weighting Factor (w_R)*. Publication 92, *Annals of the ICRP*, Vol. 33, No. 4, Pergamon Press, Oxford, 1991.
38. A. M. Kellerer and K. Hahn, Considerations on a revision of the quality factor. *Radiat. Res.* **114**, 480–488 (1988).
39. ICRP, *The 2007 Recommendations of the International Commission on Radiological Protection*. Publication 103, *Annals of the ICRP*, Vol. 37, Nos. 2–4, Elsevier, Amsterdam, 2007.
40. J. J. DeMarco, C. H. Cagnon, D. D. Cody, D. M. Stevens, C. H. McCollough, M. Zankl, E. Angel and M. F. McNitt-Gray, Estimating radiation doses from multidetector CT using Monte Carlo simulations: effects of different size voxelized patient models on magnitudes of organ and effective dose. *Phys. Med. Biol.* **52**, 2583–2597 (2007).